Acta Crystallographica Section A
Foundations of Crystallography
ISSN 0108-7673

Received 11 April 2008
Accepted 10 July 2008

X-ray and γ-ray propagation in bent crystals with flat and cylindrical surfaces

A. Apolloni,[a,b]* G. Mana,[c] C. Palmisano[d,a] and G. Zosi[a]

[a]Università di Torino, Dipartimento di Fisica Generale 'A. Avogadro', via P. Giuria 1, Torino, Italy, [b]NDSSL – Network Dynamics and Simulation Science Laboratory, Virginia Bioinformatics Institute, Virginia Polytechnic Institute and State University, Research Building XV (0477), 1880 Pratt Drive, Blacksburg, VA, USA, [c]INRiM – Istituto Nazionale di Ricerca Metrologica, Strada delle Cacce 91, Torino, Italy, and [d]Museo Storico della Fisica e Centro Studi e Ricerche 'Enrico Fermi', Compendio Viminale, 00184 Roma, Italy. Correspondence e-mail: apolloni@vbi.vt.edu

In this paper, X-ray and γ-ray propagation in crystals having a constant strain gradient and flat or cylindrical surfaces is investigated. When a displacement field is present, the Takagi–Taupin equations are solved either by the Riemann–Green method or by a numerical method. The results are applied to study the operation of a double-crystal Laue–Laue diffractometer having a flat collimating crystal followed by a bent analyzer crystal. In particular, the effect of the analyzer strain on the location of the diffraction peaks in the dispersive and non-dispersive set-up is examined, thus confirming the previously reported peak location as being set only by the diffracting-plane spacing on the analyzer entrance surface.

1. Introduction

The main purpose of this paper is to verify the soundness of our previously published work (Mana *et al.*, 2004*a*,*b*). On that occasion we studied how a constant strain gradient in the rotating crystal of a double-crystal diffractometer affects the instrument operation. The result of that investigation showed that the position of the Bragg peaks depends only on the diffracting-plane spacing on the crystal entrance surface. However, to simplify the problem, we had then assumed that all the crystal surfaces were rigorously flat. Since subsequent experiments, using cylindrically bent crystals and both X- and γ-rays to test that rather surprising result, delivered contradictory results that are still under examination (Kessler, 2007; Massa *et al.*, 2005), we were urged to investigate propagation in bent crystals in more detail. An additional reason was due to the interest in efficient Laue–Laue bent-crystal diffractometers for γ-ray spectroscopy of nuclei having a very high thermal neutron cross section (Materna *et al.*, 2006).

For these reasons we extend here our previous analysis by taking account of the curvature of the crystal surfaces and by simulating diffraction in both the non-dispersive and dispersive set-ups. In §2 we solve, using the Riemann–Green method in Cartesian coordinates, the Takagi–Taupin equations for the propagation of X- and γ-rays in bent crystals; we indicate also how the crystal surfaces are modelled, what choice of the reference perfect lattice we have adopted and what kinds of distortion of the cylindrically bent crystal we have considered. §3.1 and §3.2 deal with two cases when the crystal surfaces, on which the initial conditions have to be assigned, are flat or cylindrical, respectively. While in the first case the solutions are known (Authier & Simon, 1968; Mana & Palmisano, 2004), and are re-examined here to illustrate our formalism, we are not aware of solutions when the crystal surface is a cylinder. In fact, in the literature the case of a curved crystal surface in the macroscopic sense is just hinted at by Takagi (1969) by means of curvilinear coordinates. Subsequently, Olekhnovich & Olekhnovich (1980) carried out the calculation of the profile function of the scattering curve for a crystal in the form of a cylinder whose size does not exceed the extinction length. Later, Thorkildsen & Larsen (1998) observed that it is, in principle, possible to obtain analytical expressions for the primary extinction factor in perfect crystals having a circular diffraction plane. Podorov & Förster (2000) have examined the case when the illuminated crystal is asymmetrically cut and elastically bent. In §4 we apply our results to a double diffractometer and, to corroborate them, in §5 we solve numerically the Takagi–Taupin equations in polar coordinates for different geometrical and physical parameters.

2. Takagi–Taupin equations for distorted crystals

In order to study X-ray propagation through a distorted crystal in the Laue case, we shall apply the Takagi–Taupin equations (Takagi, 1962, 1969; Taupin, 1964; Authier, 2001; Mana & Montanari, 2004) in the two-wave approximation of the dynamical theory of X-ray diffraction. Since only cylindrical geometries will be considered, we shall use a two-dimensional model with a reference frame having the x and z axes lying in the reflection plane. Lattice distortion is described by the displacement field $\mathbf{u}(x, z)$, which gives the difference between the actual distorted lattice and a reference

perfect lattice identified by the reciprocal vector $\mathbf{h}_0$, which will be chosen at our convenience. Hence, we anchor the reference frame to it and set the x axis parallel or antiparallel to $\mathbf{h}_0$. If now we introduce the following Ewald expansion for the dielectric displacement vector $\mathbf{D} = D\hat{\mathbf{y}}$, in σ polarization,

$$D = D_o \exp(i\mathbf{K}_o \cdot \mathbf{r}) + D_h \exp\left[i(\mathbf{K}_h \cdot \mathbf{r} - \mathbf{h}_0 \cdot \mathbf{u})\right], \quad (1)$$

where D_o and D_h are slowly varying amplitudes, the Takagi–Taupin equations can be written as

$$-i\hat{\mathbf{s}}_o \cdot \nabla D_o = \frac{K\chi_o}{2} D_o + \frac{K\chi_{-h}}{2} D_h, \quad (2a)$$

$$-i\hat{\mathbf{s}}_h \cdot \nabla D_h = \frac{K\chi_o}{2} D_h + \frac{K\chi_h}{2} D_o + \left[\hat{\mathbf{s}}_h \cdot \nabla(\mathbf{h}_0 \cdot \mathbf{u})\right] D_h. \quad (2b)$$

In equations (2*a*) and (2*b*),

$$\hat{\mathbf{s}}_o = \hat{\mathbf{K}}_o = -\hat{\mathbf{x}} \sin\theta_B + \hat{\mathbf{z}} \cos\theta_B, \quad (3a)$$

$$\hat{\mathbf{s}}_h = \hat{\mathbf{K}}_h = \hat{\mathbf{x}} \sin\theta_B + \hat{\mathbf{z}} \cos\theta_B \quad (3b)$$

are the unit propagation vectors, $\mathbf{h}_0 = \hat{\mathbf{x}} 2K \sin\theta_B$, $\mathbf{K}_h = \mathbf{K}_o + \mathbf{h}_0$, $K = \|\mathbf{K}_o\| = \|\mathbf{K}_h\| = 2\pi\nu/c$ is the modulus of the wavenumber vector $\mathbf{K}_e$ of the incoming radiation (with frequency ν), θ_B is the Bragg angle (with a sign), and the complex parameters χ_o, χ_h and χ_{-h} are the Fourier components of electric susceptibility; in our case $\chi_{-h} = \chi_h$. The usual resonance term $\beta_h = K\Delta\theta \sin 2\theta_B$, where $\Delta\theta$ indicates the departure angle from Bragg's law, is not included in equation (2*b*); the reason for this lies in our particular choice of the z-axis direction. Often it is set orthogonal to the crystal surface because, in such a way, the boundary conditions for the amplitudes at the entrance surface are easily imposed. Hence, if the Bragg planes are not orthogonal to the crystal surface (asymmetric Laue case), the β_h term appears in the right-hand side of equation (2*b*). However, nothing prevents us from choosing the z axis differently, for instance, to make the reference perfect lattice resonance error equal to zero. For a flat crystal this choice may appear inconvenient but, as we generally want to consider arbitrary non-flat surfaces, it does not add additional complications. Furthermore, it is worth noting that also in the asymmetric Laue case we can consider a reference perfect lattice whose Bragg planes are orthogonal to the crystal surface, so that, in the perfect crystal equations, the resonance error is zero. However, the real Bragg planes are now deformed, that is, tilted, and the resonance error reappears as a deformation term in equation (2*b*).

We shall consider an infinite crystal slab, the surfaces of which are smooth curves (Fig. 1), with arbitrary, C^1 and bijective parametrization, that we denote Γ on the entrance surface and Σ on the exit surface. By imposing that at each point of the entrance surface the o component of the Ewald expansion [equation (1)] is equal to the incoming wave $D_e(x, z) = A(x, z)\exp(i\mathbf{K}_e \cdot \mathbf{r})$, the initial conditions for solving equations (2*a*) and (2*b*) are therefore

$$D_o(x, z)|_\Gamma = \Phi(x, z)|_\Gamma, \quad (4a)$$

$$D_h(x, z)|_\Gamma = 0, \quad (4b)$$

where $\Phi(x, z) = A(x, z)\exp[i(\mathbf{K}_e - \mathbf{K}_o) \cdot \mathbf{r}]$.

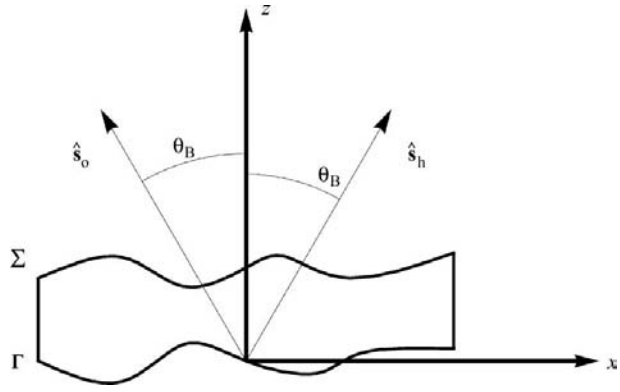

Figure 1
Example of smooth sections describing the entrance surface (Γ) and the exit surface (Σ) in the reference and/or analyzer crystal.

Equations (2*a*) and (2*b*) can be simplified by introducing two new amplitudes, d_o and d_h, defined as

$$d_{o,h} = \exp\left(-i\frac{K\chi_o}{2}\frac{\hat{\mathbf{s}}_o + \hat{\mathbf{s}}_h}{1 + \hat{\mathbf{s}}_o \cdot \hat{\mathbf{s}}_h} \cdot \mathbf{r}\right) D_{o,h}. \quad (5)$$

By substituting (5) for $D_{o,h}$ into (2*a*) and (2*b*) we obtain

$$-i\hat{\mathbf{s}}_o \cdot \nabla d_o = \frac{K\chi_{-h}}{2} d_h, \quad (6a)$$

$$-i\hat{\mathbf{s}}_h \cdot \nabla d_h = \frac{K\chi_h}{2} d_o + \left[\hat{\mathbf{s}}_h \cdot \nabla(\mathbf{h}_0 \cdot \mathbf{u})\right] d_h, \quad (6b)$$

with the initial conditions

$$d_o(x, z)|_\Gamma = \exp\left(-i\frac{K\chi_o}{2}\frac{\hat{\mathbf{s}}_o + \hat{\mathbf{s}}_h}{1 + \hat{\mathbf{s}}_o \cdot \hat{\mathbf{s}}_h} \cdot \mathbf{r}\right) \Phi(x, z)|_\Gamma, \quad (7a)$$

$$d_h(x, z)|_\Gamma = 0. \quad (7b)$$

As in the cylindrical crystals the geometry is somewhat elaborate, in the following subsections we illustrate the main underlying assumptions.

2.1. Crystal surfaces

Let us now exemplify how cylindrical surfaces are modelled. The curvature centre can be located either on the source side or on the opposite side, with R_0 and $R_0 + T$ (T denoting the crystal thickness) being the curvature radii of the entrance surface, respectively. A crystal having cylindrical surfaces will be called concave (Fig. 2, left) when its concavity is towards the source, and convex otherwise (Fig. 2, right); the position of the source is the same as shown in Fig. 3.

In the concave case, by locating the reference-frame origin at the curvature centre and omitting the double-prime symbols on x and z, the parametric components of the surfaces are

$$\begin{cases} \Gamma_x(\tau) = R_0 \sin\tau \\ \Gamma_z(\tau) = R_0 \cos\tau \end{cases} \quad (8)$$

$$\begin{cases} \Sigma_x(\sigma) = (R_0 + T)\sin\sigma \\ \Sigma_z(\sigma) = (R_0 + T)\cos\sigma \end{cases}, \quad (9)$$

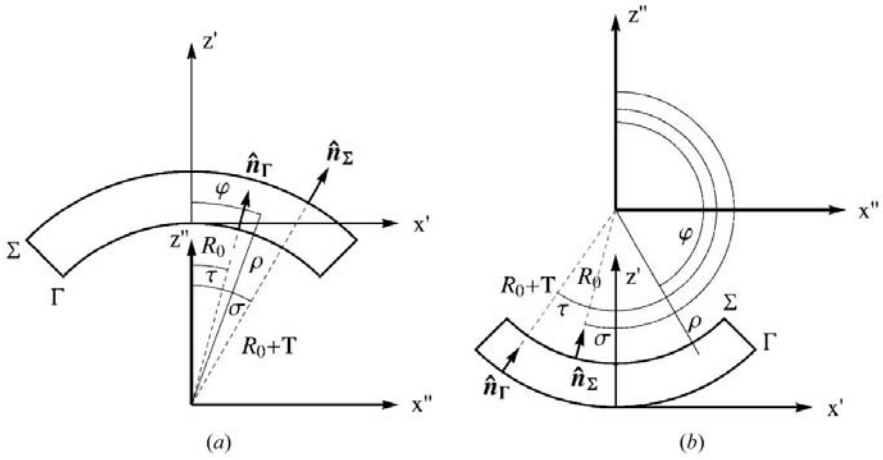

Figure 2
Two different frame references are shown, concerning the entrance surface (x', z') and the centre of curvature of the analyzer crystal (x'', z''), respectively; concave case (left) and convex case (right).

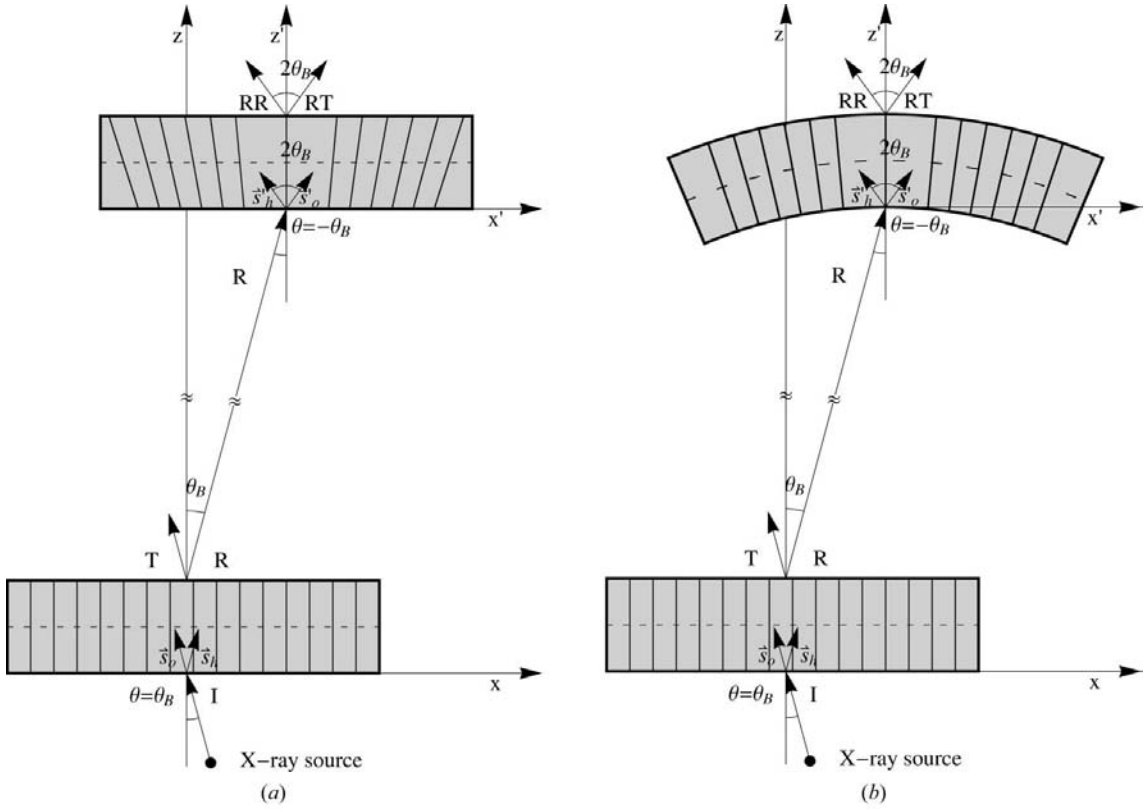

Figure 3
Layout of a two-crystal diffractometer in non-dispersive geometry. On the left, the analyzer crystal surface is flat and on the right it is cylindrically bent. The symbol I indicates the incident beam, T and R are the beams transmitted and reflected, respectively, by the collimating crystal, and RT and RR are the beams transmitted and reflected, respectively, by the crystal. The unit vectors $\hat{\mathbf{s}}_{o,h}$ are defined in equations (3*a*) and (3*b*). The angle of incidence θ is positive ($\theta = \theta_B$) on the collimating crystal and negative ($\theta = -\theta_B$) on the analyzer crystal.

where $\tau \in [\tau_1,\ \tau_2]$ and $\sigma \in [\sigma_1,\ \sigma_2]$. In the convex case, by locating the reference-frame origin again at the curvature centre, the surface components are

$$\begin{cases} \Gamma_x(\tau) = (R_0 + T)\sin\tau \\ \Gamma_z(\tau) = (R_0 + T)\cos\tau \end{cases}, \tag{10}$$

$$\begin{cases} \Sigma_x(\sigma) = R_0 \sin\sigma \\ \Sigma_z(\sigma) = R_0 \cos\sigma \end{cases}, \tag{11}$$

where $\tau \in [\pi + \tau_1,\ \pi + \tau_2]$ and $\sigma \in [\pi + \sigma_1,\ \pi + \sigma_2]$. In both cases (concave and convex), the inward and outward normals to the entrance and exit surfaces are, respectively,

$$\begin{cases} (\hat{\mathbf{n}}_\Gamma)_x(\tau) = \sin\tau \\ (\hat{\mathbf{n}}_\Gamma)_z(\tau) = \cos\tau \end{cases} \tag{12}$$

and

$$\begin{cases} (\hat{\mathbf{n}}_\Sigma)_x(\sigma) = \sin\sigma \\ (\hat{\mathbf{n}}_\Sigma)_z(\sigma) = \cos\sigma \end{cases}. \tag{13}$$

2.2. Crystal rotation

With a rotated crystal, since the reference perfect lattice can be chosen at our convenience, we make it immovable, no matter what the crystal rotation might be; consequently, a rotation is nothing more than a very special kind of distortion. Hence, our *Ansätze* to study X-ray propagation in a rotated crystal are firstly, $\mathbf{h}_0$ is independent of rotations; secondly, the rotation term, the origin of the reference frame being on the entrance surface,

$$\mathbf{u}^{\rm rot}(x,z) = (\hat{\mathbf{x}},\hat{\mathbf{z}})\left[\begin{pmatrix}\cos\alpha & \sin\alpha\\ -\sin\alpha & \cos\alpha\end{pmatrix} - \begin{pmatrix}1 & 0\\ 0 & 1\end{pmatrix}\right]\begin{pmatrix}x\\ z\end{pmatrix}$$

reduces to

$$\mathbf{u}^{\rm rot}(x,z) \simeq \alpha z\hat{\mathbf{x}} - \alpha x\hat{\mathbf{z}}, \tag{14}$$

where α is the rotation angle (clockwise oriented); and, thirdly, the crystal surfaces are left unchanged by rotations. Here the α term plays the same role as $\Delta\theta$ in the resonance error $\beta_{\rm h}$.

2.3. Lattice distortion

We shall consider two distortions, $\mathbf{u}^{\rm fan,1}(x,z)$ and $\mathbf{u}^{\rm fan,2}(x,z)$, describing cylindrically bent crystals according to the finite-element simulation (Mana *et al.*, 2004*a*). If we exclude the term $u_z^{{\rm fan},i}(x,z)\hat{\mathbf{z}}$, which is orthogonal to $\mathbf{h}_0$, we have two pure displacements in the x direction: fan-down,

$$\mathbf{u}^{\rm fan,1}(x,z) = \frac{x(z-z_{\rm m})}{R_0+z_{\rm m}}\hat{\mathbf{x}}, \tag{15a}$$

and fan-up,

$$\mathbf{u}^{\rm fan,2}(x,z) = \frac{x(z_{\rm m}-z)}{R_0+z_{\rm m}}\hat{\mathbf{x}}, \tag{15b}$$

where $z_{\rm m} = T/2$. We have chosen the x axis (now coincident with the x' axis in Fig. 2 or in the upper part of Fig. 3) and the reference perfect lattice so that $\mathbf{u}^{{\rm fan},i}(x,z_{\rm m}) = 0$. In (15*a*) the displacement is such that all the lattice planes are directed towards a point at distance R_0 from the entrance surface and the points at $z = z_{\rm m}$ are undisplaced (left upper part of Fig. 3). In (15*b*) the lattice planes are directed towards a point at distance R_0 from the exit surface. For a rotated crystal, the total displacement field $\mathbf{u}^{{\rm tot},i}(x,z)$, including both equations (15*a*) and (14), and omitting the $\hat{\mathbf{z}}$ components, is

$$\begin{aligned}\mathbf{u}^{{\rm tot},i}(x,z) &= \mathbf{u}^{{\rm fan},i}(x,z) + \mathbf{u}^{\rm rot}(x,z)\\ &= g(i)\frac{x(z-z_{\rm m})}{R_0+z_{\rm m}}\hat{\mathbf{x}} + \alpha z\,\hat{\mathbf{x}},\end{aligned} \tag{16}$$

where $g(1) = 1$, $g(2) = -1$, and the approximation $u_x^{{\rm fan},i}(x,z)\cos\alpha \simeq u_x^{{\rm fan},i}(x,z)$ is applied.

3. Propagation in distorted crystals

Equations (15*a*) and (15*b*) approximate the displacement field, characterized by a constant strain gradient, in crystals having their surfaces flat or cylindrical.

3.1. Flat crystal surfaces

In the simplest case of flat external crystal surfaces (Fig. 3, upper left), the Takagi–Taupin equations are

$$-\sin\theta_{\rm B}\frac{\partial d_{\rm o}^{(i)}}{\partial x} + \cos\theta_{\rm B}\frac{\partial d_{\rm o}^{(i)}}{\partial z} = i\frac{K\chi_{-{\rm h}}}{2}d_{\rm h}^{(i)} \tag{17a}$$

$$\begin{aligned}\sin\theta_{\rm B}\frac{\partial d_{\rm h}^{(i)}}{\partial x} + \cos\theta_{\rm B}\frac{\partial d_{\rm h}^{(i)}}{\partial z} =\\ i\frac{K\chi_{\rm h}}{2}d_{\rm o}^{(i)} + i2K\sin\theta_{\rm B}\left\{g(i)\frac{(z-z_{\rm m})}{R_0+z_{\rm m}}\sin\theta_{\rm B}\right.\\ \left. + \left[g(i)\frac{x}{R_0+z_{\rm m}} + \alpha\right]\cos\theta_{\rm B}\right\}d_{\rm h}^{(i)}\end{aligned} \tag{17b}$$

with the initial conditions

$$d_{\rm o}^{(i)}(x,0) = \Phi(x), \tag{18a}$$

$$d_{\rm h}^{(i)}(x,0) = 0, \tag{18b}$$

where we dropped the prime on x and z and we assumed that the external crystal surfaces were orthogonal to $\hat{\mathbf{s}}_{\rm o} + \hat{\mathbf{s}}_{\rm h}$ (symmetrical Laue geometry).

The coupled equations (17*a*) and (17*b*) can be simplified by a change of dependent variables. Let us introduce the two unknowns $\tilde{D}_{\rm o}^{(i)}$ and $\tilde{D}_{\rm h}^{(i)}$ defined by the expression

$$\tilde{D}_{\rm o,h}^{(i)} = \exp\left[-if^{(i)}2K\sin\theta_{\rm B}\right]d_{\rm o,h}^{(i)}, \tag{19}$$

where the function $f^{(i)}(x,z)$ is defined as

$$\begin{aligned}f^{(i)}(x,z) = \; & g(i)\frac{1}{R_0+z_{\rm m}}\left[\frac{1}{4}\left(\frac{x}{\sin\theta_{\rm B}} + \frac{z}{\cos\theta_{\rm B}}\right)^2\sin\theta_{\rm B}\cos\theta_{\rm B}\right.\\ & \left. - \frac{z_{\rm m}}{2}\left(\frac{x}{\sin\theta_{\rm B}} + \frac{z}{\cos\theta_{\rm B}}\right)\sin\theta_{\rm B}\right]\\ & + \frac{\alpha}{2}\left(\frac{x}{\sin\theta_{\rm B}} + \frac{z}{\cos\theta_{\rm B}}\right)\cos\theta_{\rm B}.\end{aligned} \tag{20}$$

If we observe that

$$\begin{aligned}\left(\sin\theta_{\rm B}\frac{\partial}{\partial x} + \cos\theta_{\rm B}\frac{\partial}{\partial z}\right)f^{(i)}(x,z) =\\ \sin\theta_{\rm B}\,g(i)\frac{(z-z_{\rm m})}{R_0+z_{\rm m}} + \cos\theta_{\rm B}\left[g(i)\frac{x}{R_0+z_{\rm m}} + \alpha\right]\end{aligned} \tag{21}$$

and

$$\left(-\sin\theta_{\rm B}\frac{\partial}{\partial x} + \cos\theta_{\rm B}\frac{\partial}{\partial z}\right)f^{(i)}(x,z) = 0, \tag{22}$$

then substitution of (19) into (17*a*) and (17*b*) gives the Takagi–Taupin equations in the unperturbed form,

$$-\sin\theta_{\rm B}\frac{\partial\tilde{D}_{\rm o}^{(i)}}{\partial x} + \cos\theta_{\rm B}\frac{\partial\tilde{D}_{\rm o}^{(i)}}{\partial z} = i\frac{K\chi_{-{\rm h}}}{2}\tilde{D}_{\rm h}^{(i)}, \tag{23a}$$

$$\sin\theta_{\rm B}\frac{\partial\tilde{D}_{\rm h}^{(i)}}{\partial x} + \cos\theta_{\rm B}\frac{\partial\tilde{D}_{\rm h}^{(i)}}{\partial z} = i\frac{K\chi_{\rm h}}{2}\tilde{D}_{\rm o}^{(i)}. \tag{23b}$$

As a consequence of equation (19), the new initial conditions on the entrance surface $z = 0$ are

$$\tilde{D}_{\rm o}^{(i)}(x,0)=\exp\left[-if^{(i)}(x,0)2K\sin\theta_{\rm B}\right]\Phi(x), \quad (24a)$$

$$\tilde{D}_{\rm h}^{(i)}(x,0)=0. \quad (24b)$$

By the Riemann–Green method (Authier & Simon, 1968; Takagi, 1969; Sommerfeld, 1964) we can find a solution by quadrature for the system [equations (23*a*), (23*b*)] with initial conditions [equations (24*a*), (24*b*)]

$$\tilde{D}_{\rm o,h}^{(i)}(x,z)=\int_{-\infty}^{+\infty}G_{\rm o,h}(x-x',z)\times\exp\left[-if^{(i)}(x',0)2K\sin\theta_{\rm B}\right]\Phi(x')\,{\rm d}x'. \quad (25)$$

Following the notation of Palmisano & Zosi (2005), the kernels $G_{\rm o}$ and $G_{\rm h}$ are

$$G_{\rm o}(x,z)=\delta(x+z\tan\theta_{\rm B})-\frac{K}{4|\sin\theta_{\rm B}|}(\chi_{\rm h}\chi_{-\rm h})^{1/2}\times{\rm H}(z|\tan\theta_{\rm B}|+x){\rm H}(z|\tan\theta_{\rm B}|-x)\times\left(\frac{z\tan\theta_{\rm B}-x}{z\tan\theta_{\rm B}+x}\right)^{1/2}\times{\rm J}_1\left[\frac{\rm K}{2|\sin\theta_{\rm B}|}(\chi_{\rm h}\chi_{-\rm h})^{1/2}\left(z^2\tan^2\theta_{\rm B}-x^2\right)^{1/2}\right] \quad (26)$$

and

$$G_{\rm h}(x,z)=\frac{i}{4}\frac{K\chi_{\rm h}}{|\sin\theta_{\rm B}|}{\rm H}(z|\tan\theta_{\rm B}|+x){\rm H}(z|\tan\theta_{\rm B}|-x)\times{\rm J}_0\left[\frac{K}{2|\sin\theta_{\rm B}|}(\chi_{\rm h}\chi_{-\rm h})^{1/2}\left(z^2\tan^2\theta_{\rm B}-x^2\right)^{1/2}\right]. \quad (27)$$

In (26) and (27), H(z) is the Heaviside function and $J_0(z)$ and $J_1(z)$ are the Bessel functions of the first kind and order 0 and 1, respectively. Therefore the solution to Takagi–Taupin equations (17*a*) and (17*b*) with initial conditions [equations (18*a*), (18*b*)] is

$$d_{\rm o,h}^{(i)}(x,z)=\exp\left[if^{(i)}(x,z)2K\sin\theta_{\rm B}\right]\int_{-\infty}^{+\infty}G_{\rm o,h}(x-x',z)\times\exp\left[-if^{(i)}(x',0)2K\sin\theta_{\rm B}\right]\Phi(x')\,{\rm d}x'. \quad (28)$$

We see from (28) that the effect of a constant strain gradient has been reduced to a similarity transformation of the $G_{\rm o}$ and $G_{\rm h}$ kernels (Mana & Palmisano, 2004). Equations (5) and (28) show that the intensities of the transmitted and diffracted beams $D_{\rm o}^{(i)}(x,z)$ and $D_{\rm h}^{(i)}(x,z)$ on the exit surface $z=T$ are

$$I_{\rm o,h}^{(i)}(\alpha)=\int_{-\infty}^{+\infty}|D_{\rm o,h}^{(i)}(x,T)|^2\cos\theta_{\rm B}\,{\rm d}x=\int_{-\infty}^{+\infty}\exp\left[-K\Im(\chi_{\rm o})T/\cos\theta_{\rm B}\right]\times\left|\int_{-\infty}^{+\infty}G_{\rm o,h}(x-x',T)\exp\left[-if^{(i)}(x',0)2K\sin\theta_{\rm B}\right]\times\Phi(x')\,{\rm d}x'\right|^2\cos\theta_{\rm B}\,{\rm d}x, \quad (29)$$

where $\Im(\chi_{\rm o})$ is the imaginary part of $\chi_{\rm o}$. Eventually, substitution of (20) into (29) gives

$$I_{\rm o,h}^{(i)}(\alpha)=\int_{-\infty}^{+\infty}\exp[-K\Im(\chi_{\rm o})T/\cos\theta_{\rm B}]\left|\int_{-\infty}^{+\infty}G_{\rm o,h}(x-x',T)\times\exp\left\{-i2K\sin\theta_{\rm B}\frac{\cos\theta_{\rm B}}{R_0+z_{\rm m}}\left[\frac{1}{4}g(i)\frac{x'^2}{\sin\theta_{\rm B}}-\frac{1}{2}x'\left(g(i)\frac{z_{\rm m}}{\cos\theta_{\rm B}}-\frac{R_0+z_{\rm m}}{\sin\theta_{\rm B}}\alpha\right)\right]\right\}\Phi(x')\,{\rm d}x'\right|^2\times\cos\theta_{\rm B}\,{\rm d}x. \quad (30)$$

Equation (30) gives the rocking curves $I_{\rm o,h}^{(i)}(\alpha)$ when the crystal is distorted by the displacement field (15*a*) or (15*b*); the external crystal surfaces are flat and $\Phi(x)$ is the complex field amplitude of a generic incoming beam. Additionally, and generally, the effect of the displacement fields [equations (15*a*), (15*b*) or (16)] on the intensity $I_{\rm o,h}^{(i)}$ in (30) is seen to consist of a phase redefinition of the initial condition $\Phi(x)$. Evaluation of (30) in the limit with R_0 tending to $+\infty$ gives the rocking curve of a perfect analyzer crystal. With the variable change $\alpha=\bar{\alpha}^{(i)}+\alpha'$, where $\bar{\alpha}^{(i)}$ is

$$\bar{\alpha}^{(i)}=g(i)\frac{z_{\rm m}}{R_0+z_{\rm m}}\tan\theta_{\rm B} \quad (31a)$$

$$=-\frac{\partial u_x^{{\rm fan},i}}{\partial x}(x,0)\tan\theta_{\rm B}, \quad (31b)$$

equation (30) can be reduced to the simpler form

$$I_{\rm o,h}^{(i)}(\bar{\alpha}^{(i)}+\alpha')=\int_{-\infty}^{+\infty}\exp\left[-K\Im(\chi_{\rm o})T/\cos\theta_{\rm B}\right]\times\left|\int_{-\infty}^{+\infty}G_{\rm o,h}(x-x',T)\times\exp\left\{-i2K\sin\theta_{\rm B}\frac{\cos\theta_{\rm B}}{R_0+z_{\rm m}}\left[\frac{1}{4}g(i)\frac{x'^2}{\sin\theta_{\rm B}}+\frac{1}{2}x'\frac{R_0+z_{\rm m}}{\sin\theta_{\rm B}}\alpha'\right]\right\}\Phi(x')\,{\rm d}x'\right|^2\cos\theta_{\rm B}\,{\rm d}x. \quad (32)$$

3.2. Cylindrical surfaces

By application of the Riemann–Green method, the solution of system (17*a*)–(17*b*), with the initial conditions (7*a*)–(7*b*), is the flux integral

$$d_{\rm o,h}^{(i)}(x,z)=\exp\left[if^{(i)}(x,z)2K\sin\theta_{\rm B}\right]\int_\Gamma G_{\rm o,h}(x-\Gamma_x,z-\Gamma_z)\times\exp\left[-if^{(i)}(\Gamma_x,\Gamma_z)2K\sin\theta_{\rm B}\right]\times\exp\left[-i\frac{K\chi_{\rm o}}{2}\frac{\hat{\mathbf{s}}_{\rm o}+\hat{\mathbf{s}}_{\rm h}}{1+\hat{\mathbf{s}}_{\rm o}\cdot\hat{\mathbf{s}}_{\rm h}}\cdot(\Gamma_x\hat{\mathbf{x}}+\Gamma_z\hat{\mathbf{z}})\right]\times\Phi(\Gamma_x,\Gamma_z)\frac{\hat{\mathbf{s}}_{\rm o}\cdot\hat{\mathbf{n}}_\Gamma}{\cos\theta_{\rm B}}\,{\rm d}\Gamma, \quad (33)$$

which generalizes (28). In (33) the prime on x and z has been omitted (see upper right part of Fig. 3), the unit vector $\hat{\mathbf{n}}_\Gamma$ is the inward normal to the Γ surface, Γ_x and Γ_z are the surface parametric components and dΓ is a shorthand form for $|{\rm d}\Gamma/{\rm d}\tau|\,{\rm d}\tau$. Let $\hat{\mathbf{n}}_\Sigma$ be the outward normal to the exit surface Σ. From (5), (33) and (20) the intensity of the forward transmitted and diffracted beams is

$$
\begin{aligned}
I^{(i)}_{\mathrm{o,h}}(\alpha) &= \int_{\Sigma} |D^{(i)}_{\mathrm{o,h}}(\Sigma)|^2 \hat{\mathbf{s}}_{\mathrm{o,h}} \cdot \hat{\mathbf{n}}_{\Sigma}\, \mathrm{d}\Sigma \\
&= \int_{\Sigma} \exp\left(-K\Im(\chi_{\mathrm{o}})\frac{\Sigma_z}{\cos\theta_{\mathrm{B}}}\right)\left|\int_{\Gamma} G_{\mathrm{o,h}}(\Sigma_x-\Gamma_x,\,\Sigma_z-\Gamma_z)\right. \\
&\quad\times \exp\left\{-\frac{i2K\sin^2\theta_{\mathrm{B}}\cos\theta_{\mathrm{B}}}{R_0+z_{\mathrm{m}}}\left[\frac{g(i)}{4}\left(\frac{\Gamma_x}{\sin\theta_{\mathrm{B}}}+\frac{\Gamma_z}{\cos\theta_{\mathrm{B}}}\right)^2\right.\right. \\
&\quad\left.\left.-\frac{1}{2}\left(\frac{\Gamma_x}{\sin\theta_{\mathrm{B}}}+\frac{\Gamma_z}{\cos\theta_{\mathrm{B}}}\right)\left(g(i)\frac{z_{\mathrm{m}}}{\cos\theta_{\mathrm{B}}}-\frac{R_0+z_{\mathrm{m}}}{\sin\theta_{\mathrm{B}}}\alpha\right)\right]\right\} \\
&\quad\times \exp\left(-i\frac{K\chi_{\mathrm{o}}}{2}\frac{\Gamma_z}{\cos\theta_{\mathrm{B}}}\right) \\
&\quad\left.\times\,\Phi(\Gamma_x,\Gamma_z)\frac{\hat{\mathbf{s}}_{\mathrm{o}}\cdot\hat{\mathbf{n}}_{\Gamma}}{\cos\theta_{\mathrm{B}}}\,\mathrm{d}\Gamma\right|^2 \hat{\mathbf{s}}_{\mathrm{o,h}}\cdot\hat{\mathbf{n}}_{\Sigma}\,\mathrm{d}\Sigma. \qquad (34)
\end{aligned}
$$

In the concave case (Fig. 2, left), by imposing the condition that the reference-frame origin is located on the entrance surface, then the parametric equations of the external surfaces Γ and Σ become

$$
\begin{cases}
\Gamma_x(\tau) = R_0\sin\tau, \\
\Gamma_z(\tau) = R_0\cos\tau - R_0
\end{cases} \qquad (35)
$$

and

$$
\begin{cases}
\Sigma_x(\sigma) = (R_0+T)\sin\sigma, \\
\Sigma_z(\sigma) = (R_0+T)\cos\sigma - R_0,
\end{cases} \qquad (36)
$$

then (34), using the definitions (31*a*), (12)–(13) and (35)–(36), can be rewritten as

$$
\begin{aligned}
I^{(1)}_{\mathrm{o,h}}\big(\bar{\boldsymbol{\alpha}}^{(1)}+\alpha'\big) &= \int_{\sigma_1}^{\sigma_2} \exp\left[-K\Im(\chi_{\mathrm{o}})\frac{(R_0+T)\cos\sigma - R_0}{\cos\theta_{\mathrm{B}}}\right] \\
&\quad\times\left|\int_{\tau_1}^{\tau_2}\exp\left(-i\frac{K\chi_{\mathrm{o}}}{2}R_0\frac{\cos\tau-1}{\cos\theta_{\mathrm{B}}}\right)\Phi\big[R_0\sin\tau,\,R_0(\cos\tau-1)\big]\right. \\
&\quad\times\exp\left\{-i2K\sin^2\theta_{\mathrm{B}}\cos\theta_{\mathrm{B}}\frac{R_0}{R_0+z_{\mathrm{m}}}\left(\frac{\sin\tau}{\sin\theta_{\mathrm{B}}}+\frac{\cos\tau-1}{\cos\theta_{\mathrm{B}}}\right)\right. \\
&\quad\left.\left.\times\left[g(1)\frac{R_0}{4}\left(\frac{\sin\tau}{\sin\theta_{\mathrm{B}}}+\frac{\cos\tau-1}{\cos\theta_{\mathrm{B}}}\right)+\frac{1}{2}\frac{R_0+z_{\mathrm{m}}}{\sin\theta_{\mathrm{B}}}\alpha'\right]\right\}\right. \\
&\quad\times G_{\mathrm{o,h}}\big[(R_0+T)\sin\sigma - R_0\sin\tau,\,(R_0+T)\cos\sigma - R_0\cos\tau\big] \\
&\quad\left.\times\frac{\cos(\theta_{\mathrm{B}}+\tau)}{\cos\theta_{\mathrm{B}}}R_0\mathrm{d}\tau\right|^2 \hat{\mathbf{s}}_{\mathrm{o,h}}\cdot\hat{\mathbf{n}}_{\Sigma}(R_0+T)\,\mathrm{d}\sigma, \qquad (37)
\end{aligned}
$$

where

$$
\hat{\mathbf{s}}_{\mathrm{o,h}}\cdot\hat{\mathbf{n}}_{\Sigma} = \begin{cases} \cos(\theta_{\mathrm{B}}+\sigma) & \text{o wave} \\ \cos(\theta_{\mathrm{B}}-\sigma) & \text{h wave.} \end{cases} \qquad (38)
$$

In the convex case (Fig. 2, right), by imposing the condition that the reference-frame origin is located on the entrance surface, the parametric equations of the external surfaces Γ and Σ become

$$
\begin{cases}
\Gamma_x(\tau) = (R_0+T)\sin\tau \\
\Gamma_z(\tau) = (R_0+T)(\cos\tau+1)
\end{cases} \qquad (39)
$$

and

$$
\begin{cases}
\Sigma_x(\sigma) = R_0\sin\sigma \\
\Sigma_z(\sigma) = R_0\cos\sigma + R_0 + T,
\end{cases} \qquad (40)
$$

then, by following the same procedure, that is, with the use of definitions (31*a*), (12)–(13) and (39)–(40), equation (34) can be rewritten as

$$
\begin{aligned}
I^{(2)}_{\mathrm{o,h}}\big(\bar{\boldsymbol{\alpha}}^{(2)}+\alpha'\big) &= \int_{\pi+\sigma_1}^{\pi+\sigma_2}\exp\left[-K\Im(\chi_{\mathrm{o}})\frac{R_0\cos\sigma+R_0+T}{\cos\theta_{\mathrm{B}}}\right] \\
&\quad\times\left|\int_{\tau_1}^{\tau_2} G_{\mathrm{o,h}}\big[R_0\sin\sigma-(R_0+T)\sin\tau,\,R_0\cos\sigma-(R_0+T)\cos\tau\big]\right. \\
&\quad\times\exp\left\{-i2K\sin^2\theta_{\mathrm{B}}\cos\theta_{\mathrm{B}}\frac{R_0+T}{R_0+z_{\mathrm{m}}}\left(\frac{\sin\tau}{\sin\theta_{\mathrm{B}}}+\frac{\cos\tau+1}{\cos\theta_{\mathrm{B}}}\right)\right. \\
&\quad\left.\left.\times\left[g(2)\frac{R_0+T}{4}\left(\frac{\sin\tau}{\sin\theta_{\mathrm{B}}}+\frac{\cos\tau+1}{\cos\theta_{\mathrm{B}}}\right)+\frac{1}{2}\frac{R_0+z_{\mathrm{m}}}{\sin\theta_{\mathrm{B}}}\alpha'\right]\right\}\right. \\
&\quad\times\exp\left[-i\frac{K\chi_{\mathrm{o}}}{2}(R_0+T)\frac{\cos\tau+1}{\cos\theta_{\mathrm{B}}}\right] \\
&\quad\times\Phi[(R_0+T)\sin\tau,\,(R_0+T)(\cos\tau+1)] \\
&\quad\left.\times\frac{\cos(\theta_{\mathrm{B}}+\tau)}{\cos\theta_{\mathrm{B}}}(R_0+T)\,\mathrm{d}\tau\right|^2 \hat{\mathbf{s}}_{\mathrm{o,h}}\cdot\hat{\mathbf{n}}_{\Sigma}R_0\,\mathrm{d}\sigma, \qquad (41)
\end{aligned}
$$

where $\hat{\mathbf{s}}_{\mathrm{o,h}}\cdot\hat{\mathbf{n}}_{\Sigma}$ has the same meaning as in (38).

4. Double-crystal diffractometer

Figs. 3 and 4 show the Laue–Laue diffractometer in both the non-dispersive and dispersive set-ups. We consider a flat collimating perfect crystal and a monochromatic point source located in $(L\sin\theta_{\mathrm{B}}, -L\cos\theta_{\mathrm{B}})$, where L is the distance between the source and the entrance point of the collimating crystal. We have chosen the vector $\mathbf{h}_0$ of the analyzer reference perfect lattice equal to the vector $\mathbf{h}_0$ of the collimating crystal; therefore, these two lattices have the same spacing, and when $\alpha = 0$ they are parallel. If the two crystals have the same lattice spacing, the analyzer rotation α between the non-dispersive and dispersive geometries is equal to $2\theta_{\mathrm{B}}$; a different rotation is related to a different lattice spacing in the collimating and analyzer crystals.

4.1. Rocking curves

Let us confine our study to the reflected beam. When we examine equation (32) we see that, if

$$
\Phi(x) = \Phi(-x), \qquad (42)
$$

where $\Phi(x)$ is the amplitude of the o component of the external field on the entrance surface of the analyzer, the intensity profile of $I^{(i)}_{\mathrm{h}}(\bar{\boldsymbol{\alpha}}^{(i)}+\alpha')$ is invariant under the $\alpha' \longleftrightarrow -\alpha'$ exchange, as can be easily checked by the double substitution $x' = -\tilde{x}'$, $x = -\tilde{x}$. This means that $I^{(i)}_{\mathrm{h}}(\alpha)$ has a vertical symmetry axis passing through $\bar{\boldsymbol{\alpha}}^{(i)}$. Let us note that (42) is fulfilled if the amplitude of the o component of the incoming beam is an even function.

The formula $\bar{\alpha}^{(i)}/\tan\theta_B = -\partial u_x^{\mathrm{fan},i}(x,0)/\partial x$, obtained from (31*b*), is our formulation of the $\Delta\theta/\tan\theta_B = -\Delta d/d$ Bragg law. It is to be noted that, if we remove the previous condition $z_m = T/2$, and additionally impose $z_m = 0$ implying $u_x^{\mathrm{fan},i}(x,0) = 0$ and, consequently, $\bar{\alpha}^{(i)} = 0$, then there is no shift of the reflection peak with respect to the perfect-crystal case. With crystals having cylindrical surfaces, when we introduce the approximations $\cos\tau \approx \cos(\theta_B+\tau) \simeq \cos(\theta_B-\tau) \simeq \cos(\theta_B-\sigma) \simeq \cos(\theta_B+\sigma) \simeq 1$ in (37) and in (41), and the symmetry requirement in (42) is satisfied, we again conclude that $I_h^{(i)}(\alpha)$ has a vertical symmetry axis passing through $\bar{\alpha}^{(i)} = g(i)\tan\theta_B\, z_m/(R_0+z_m)$. The profiles obtained numerically, without any approximation as we shall shortly discuss in §5, are symmetric and validate the above approximation. Mana *et al.* (2004*a*) report that, in the presence of a constant strain gradient in the analyzer, the Laue–Laue rocking curve is shifted by $(\Delta d/d)\tan\theta_B$, where the lattice strain is evaluated on the crystal surface. However, this peak shift is not easily measurable. Since the analyzer rotation between dispersive and non-dispersive reflection peaks is an experimentally observable quantity, we give now the relevant equation. In our formalism, the o component of the analyzer crystal field co-propagates or counterpropagates with respect to the x axis according to the sign of θ_B; therefore, the exchange between the dispersive and non-dispersive geometries corresponds to the substitution of $-\theta_B$ for θ_B. If we observe that the non-dispersive rocking curve peaks when $\alpha = \bar{\alpha}^{(i)}(-\theta_B)$, where θ_B is the Bragg angle for the collimating crystal (Fig. 3), and we observe as well that the dispersive one peaks when $\alpha = 2\theta_B + \bar{\alpha}^{(i)}(\theta_B)$ (Fig. 4), the sought formula is

$$\Delta\alpha^{(i)} = 2\theta_B + \bar{\alpha}^{(i)}(\theta_B) - \bar{\alpha}^{(i)}(-\theta_B) \quad (43a)$$

$$= 2\left[\theta_B + \bar{\alpha}^{(i)}(\theta_B)\right] \quad (43b)$$

$$= 2\left[\theta_B - \frac{\partial u_x^{\mathrm{fan},i}}{\partial x}(x,0)\tan\theta_B\right], \quad (43c)$$

where $(\partial u_x^{\mathrm{fan},i}/\partial x)(x,0)$ is the lattice strain on the analyzer entrance surface.

5. Numerical simulation

In order to validate our previous results we have also studied the diffractometer operation by solving the Takagi–Taupin equations numerically. Again we consider the two distinct

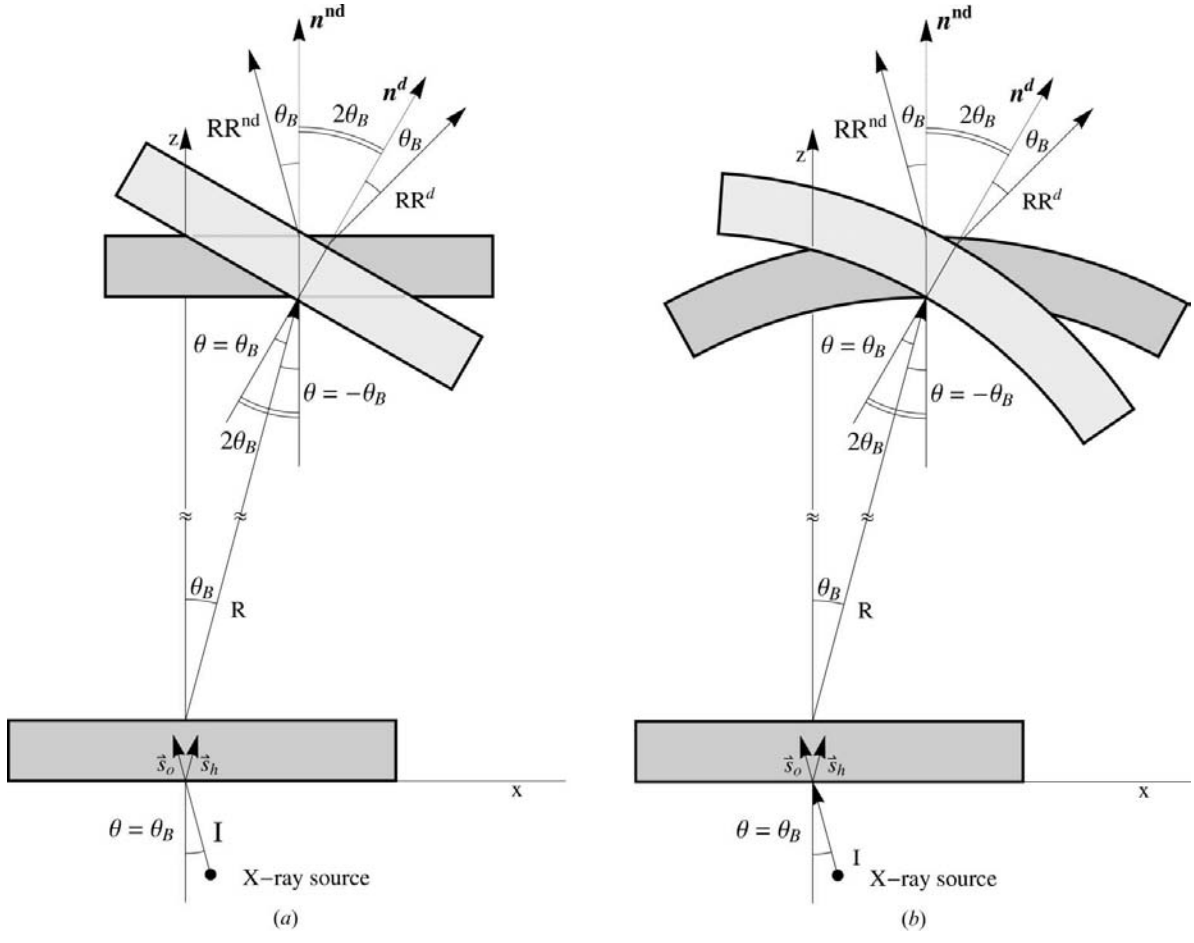

Figure 4
Layout of a two-crystal diffractometer in non-dispersive and dispersive geometries. The symbol I indicates the incident beam, R is the beam reflected by the collimating crystal, RR^{nd} and RR^{d} are the double reflected outgoing beams, the superscripts 'nd' and 'd' refer to the non-dispersive and dispersive set-up, respectively. The unit vectors $\hat{\mathbf{s}}_{o,h}$ are defined in equations (3*a*) and (3*b*). The angle of incidence θ on the collimating crystal is positive ($\theta = \theta_B$); the angle of incidence θ on the analyzer crystal is negative for the non-dispersive set-up and positive for the dispersive set-up.

Table 1
Parameters used for different energies.

Reference	T (mm)	L (m)	$w/2$ (μm)	E (keV)	R_0 (m)
Mana *et al.* (2004*a*)	0.5	1	50	17	160
Massa *et al.* (2005)	2.5	16	500	184	697

cases of flat or cylindrical analyzer surfaces. The collimating crystal is a parallel-sided silicon slab limited by two surfaces orthogonal to the (220) Bragg planes. The X- or γ-ray source illuminates the collimating crystal by a monochromatic cylindrical wave $D_e(x, z) = A(x, z)\exp(i\mathbf{K}_o \cdot \mathbf{r})$, where

$$A(x,0) = \begin{cases} \Lambda(x)[x-(w/2)]^8[x+(w/2)]^8/(w/2)^{16} & \text{if } -\tfrac{w}{2} \le x \le \tfrac{w}{2} \\ 0 \quad \text{otherwise,} \end{cases} \tag{44}$$

$$\Lambda(x) = \frac{1}{4\pi L}\exp\left(i\frac{2\pi}{\lambda}\frac{\cos^2\theta_B}{2L}x^2\right), \tag{45}$$

$\lambda = hc/E$ (where E is the photon energy) is the wavelength, $w/2$ is the half-width on the entrance slit, and the Bragg angle is positive. The exponents 8 and 16 in (44) render it possible for the function to have a high order of differentiability, making the boundary conditions smooth and the numerical computations easier. The expression in (45) can be found in Authier & Simon (1968). In the numerical simulation we considered the two sets of parameters shown in Table 1; the lower-energy value refers to the experimental set-up described by Mana *et al.* (2004*a*), the upper by Massa *et al.* (2005). We have considered silicon (220) Bragg planes and have taken the values of the dielectric susceptibilities from Sergey Stepanov's X-ray Server (http://sergey.gmca.aps.anl.gov/).

As a first step we solved (17*a*) and (17*b*) for a perfect crystal with boundary conditions [equation (44)]. Subsequently, the reflected beam, which we shall indicate by $D_h^{col}(x, T)$, was free-propagated rigidly from the collimating crystal onto the entrance surface of the analyzer crystal.

5.1. Flat analyzer surfaces

In this case (see Fig. 3, left) the propagation equations of the analyzer fields $d_o^{ana,\,i}(x', z')$ and $d_h^{ana,\,i}(x', z')$ are equations (17*a*) and (17*b*), where $u_{x'}^{fan,i}(x', z')$ is the displacement field in (15*a*) and (15*b*), the Bragg angle is negative, and the initial field values are

$$d_o^{ana,\,i}(x', 0) = d_h^{col}(x', T), \tag{46a}$$

$$d_h^{ana,\,i}(x', 0) = 0, \tag{46b}$$

where, in the right-hand side of (46*a*), the translation of $d_h^{col}(x, T)$ along the x axis and the shift of the new reference-frame origin, on the analyzer entrance surface, cancel each other. In general, the amplitude in the (x, z) reference frame of the h wave exiting ($z \ge T$) from the collimator, and rigidly moving along $\hat{\mathbf{s}}_h$ without any wavefront distortion, is given by

$$d_h^{col}(x, z) = d_h^{col}\big[x - (z - T)\big|\tan\theta_B\big|, T\big]. \tag{47}$$

We have calculated the numerical solutions with the aid of *Mathematica* (Wolfram Research, 2007); we have obtained the same results (to within 0.1%) by performing the integration in (28) numerically. In Figs. 5 and 6 we show the rocking curves when the analyzer distortion corresponds to the fan-down and fan-up cases, in both the non-dispersive and dispersive geometries; the peak shifts agree with the values predicted by (31*a*).

In Fig. 7 we have expanded the range on the μrad axis, when no displacement field is present, just to show that the wings of the upper curve also decrease asymptotically, although more slowly. Two cases, calculated numerically and according to (31*a*), are compared in Fig. 8, showing that the maximum difference in $\Delta\alpha$ amounts to a few parts per 10^{-7}. Figs. 5 and 6 require a few comments. Firstly, in contrast to experimental observations, there is no spreading in Fig. 6; the reason for this is that we assumed the source to be monochromatic and we did not integrate over its linewidth.

In a non-dispersive geometry, with a perfect-crystal analyzer having the same lattice spacing as the collimating crystal, all rocking curves peak when $\alpha = 0$, no matter what the wavelength might be. On the contrary, in a dispersive geometry the rocking curves peak when $\alpha = 2\theta_B(\lambda)$, thus giving rise to a convolution integral. Secondly, we did not pay particular attention to the crystal-field intensities; therefore, the relative intensities of the 17 keV and 184 keV plots are meaningless and the two curves are not comparable. Finally, the dotted lines show only the central part of the extremely wide 17 keV curve.

5.2. Cylindrical analyzer surfaces

In this case, we rewrote the Takagi–Taupin equations (17*a*) and (17*b*) using polar coordinates, the reference-frame origin being in the centre of curvature of the entrance surface Γ. Hence, the new coordinates are (Fig. 2)

$$\rho = \left(x''^2 + z''^2\right)^{1/2}, \tag{48a}$$

$$\varphi = \begin{cases} \arctan(x''/z'') & z'' > 0 \\ \pi/2 & z'' = 0,\ x'' > 0, \\ \pi + \arctan(x''/z'') & z'' < 0 \end{cases} \tag{48b}$$

and the equations become

$$\cos(\theta_B + \varphi)\frac{\partial d_o^{ana,\,i}}{\partial\rho} - \frac{\sin(\theta_B + \varphi)}{\rho}\frac{\partial d_o^{ana,\,i}}{\partial\varphi} = i\frac{K\chi_{-h}}{2}d_h^{ana,\,i} \tag{49a}$$

$$\cos(\theta_B - \varphi)\frac{\partial d_h^{ana,i}}{\partial\rho} + \frac{\sin(\theta_B - \varphi)}{\rho}\frac{\partial d_h^{ana,i}}{\partial\varphi} = i\frac{K\chi_h}{2}d_o^{ana,i} + i2K\sin\theta_B\left[\cos(\theta_B - \varphi)\frac{\partial u_x^{(i)}}{\partial\rho} + \frac{\sin(\theta_B - \varphi)}{\rho}\frac{\partial u_x^{(i)}}{\partial\varphi}\right]d_h^{ana,i}, \tag{49b}$$

where the Bragg angle θ_B is negative in the non-dispersive case and positive in the dispersive one. In the concave case the old coordinates (x', z') in terms of (x'', z'') are given by (Fig. 2, left)

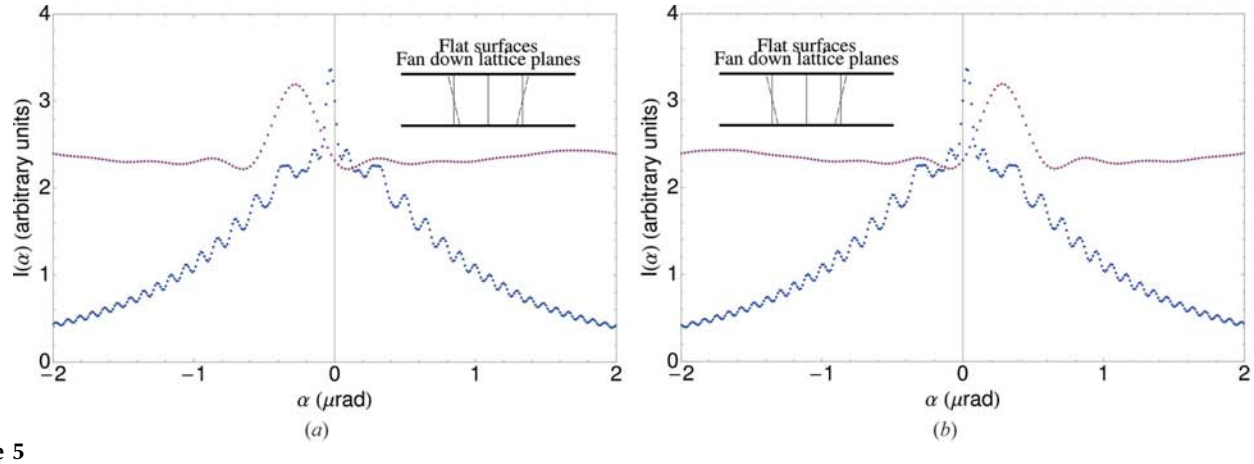

Figure 5
Non-dispersive (left) and dispersive (right) rocking curves for a flat Si analyzer with a fan-down distortion. Upper and lower curves refer to energies of 17 keV and 184 keV, respectively. Bragg planes are (220) and the relevant parameter values are given in Table 1.

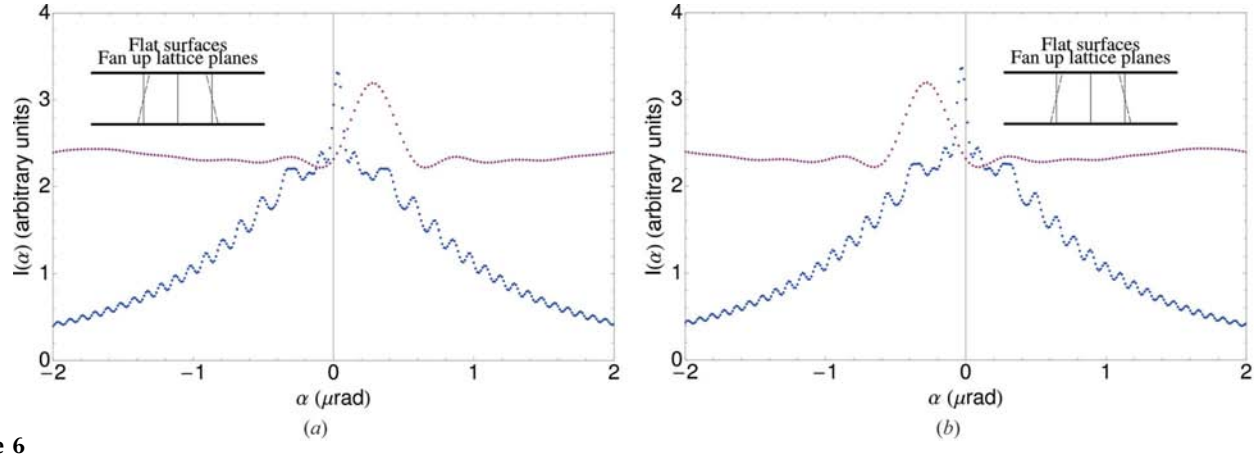

Figure 6
Non-dispersive (left) and dispersive (right) rocking curves for a flat Si analyzer with a fan-up distortion. Upper and lower curves refer to the energies of 17 keV and 184 keV, respectively. Bragg planes are (220) and the relevant parameter values are given in Table 1.

$$\begin{cases} x' = x'' = \rho \sin\varphi \\ z' = z'' - R_0 = \rho\cos\varphi - R_0 \end{cases} \tag{50}$$

and in the convex case the old coordinates (x', z') are given by (Fig. 2, right)

$$\begin{cases} x' = x'' = \rho \sin\varphi \\ z' = z'' + R_0 + T = \rho\cos\varphi + R_0 + T. \end{cases} \tag{51}$$

The x'' components of the total displacement fields $\mathbf{u}^{\mathrm{tot},1}(\rho, \varphi)$ and $\mathbf{u}^{\mathrm{tot},2}(\rho, \varphi)$ in (16) are

$$u_{x''}^{\mathrm{tot},1}(\rho,\varphi) = g(1)\left(\frac{\rho\cos\varphi - R_0 - z_\mathrm{m}}{R_0 + z_\mathrm{m}}\right)\rho\sin\varphi + \alpha(\rho\cos\varphi - R_0) \tag{52}$$

and

$$u_{x''}^{\mathrm{tot},2}(\rho,\varphi) = g(2)\left(\frac{\rho\cos\varphi + R_0 + z_\mathrm{m}}{R_0 + z_\mathrm{m}}\right)\rho\sin\varphi + \alpha(\rho\cos\varphi + R_0 + T), \tag{53}$$

which can be rewritten as

$$u_{x''}^{\mathrm{tot},i}(\rho,\varphi) = \rho\sin\varphi\left[g(i)\frac{\rho\cos\varphi}{R_0 + z_\mathrm{m}} - 1\right] + \alpha\rho\cos\varphi, \tag{54}$$

the constant α terms being omitted. From (7*a*), (7*b*), (47), (50) and (51), the boundary conditions for the concave case are

$$d_\mathrm{o}^{\mathrm{ana},1}(R_0,\varphi) = \exp\left(-i\frac{K\chi_\mathrm{o}}{2}R_0\frac{\cos\varphi - 1}{\cos\theta_\mathrm{B}}\right) d_\mathrm{h}^{\mathrm{col}}\big[R_0\sin\varphi + R_0(\cos\varphi - 1)\tan\theta_\mathrm{B}, T\big], \tag{55a}$$

$$d_\mathrm{h}^{\mathrm{ana},1}(R_0,\varphi) = 0, \tag{55b}$$

and

$$d_\mathrm{o}^{\mathrm{ana},2}(R_0 + T,\varphi) = \exp\left[-i\frac{K\chi_\mathrm{o}}{2}(R_0 + T)\frac{\cos\varphi + 1}{\cos\theta_\mathrm{B}}\right] \times d_\mathrm{h}^{\mathrm{col}}\big\{(R_0 + T)\big[\sin\varphi + (1 + \cos\varphi)\tan\theta_\mathrm{B}\big], T\big\}, \tag{56a}$$

$$d_\mathrm{h}^{\mathrm{ana},2}(R_0 + T,\varphi) = 0 \tag{56b}$$

for the convex case. Here, too, the numerical solution of (49*a*) and (49*b*) agrees with the numerical integration of (33).

Figs. 9 and 10 show the rocking curves for a concave and for a convex crystal, respectively, in the non-dispersive and

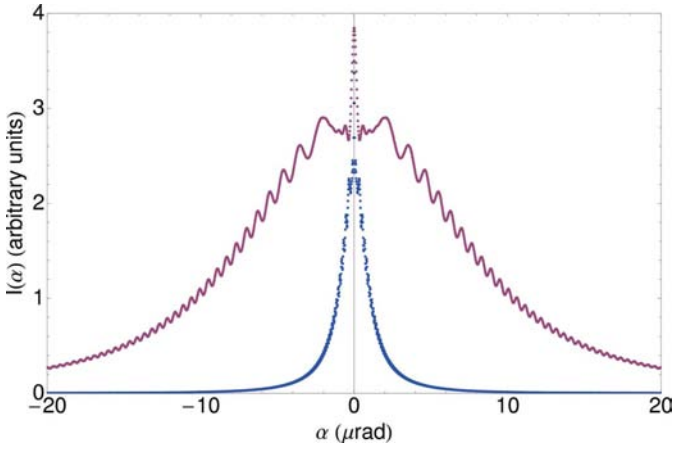

Figure 7
Non-dispersive rocking curves. The larger profile refers to the Mo wavelength and the other to 184 keV. The horizontal range, −20 μrad to 20 μrad, is expanded with respect to the previous −2 μrad to 2 μrad to show the asymptotic behaviour of both rocking curves.

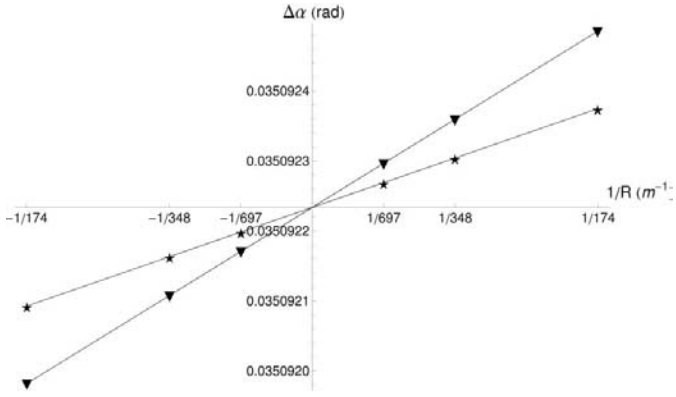

Figure 8
Analyzer rotation $\Delta\alpha$ from non-dispersive to dispersive geometry as a function of curvature $1/R$ for T = 1.4 mm (black down triangles), T = 2.5 mm (stars) when E = 184 keV. Positive and negative values of $1/R$ refer to the concave and convex cases, respectively, and have been calculated numerically.

dispersive geometries. Also in this case the peak shifts agree with the values obtained from (32*a*). By comparing the profiles in Figs. 5 and 9 we observe a slight effect depending on the surface curvature which, anyway, does not alter their symmetry; furthermore, the wings of the upper curves do not appear in the range shown; the same can be concluded from Figs. 6 and 10.

Additionally, the figures exemplify that peak shifts, and consequently $\Delta\alpha$, are independent of the surface geometry (flat or cylindrical, concave or convex), but they depend only on the entrance-surface strain $\Delta d/d$. This confirms that the flat-surface approximation used by Mana *et al.* (2004*a*) was admissible. To check further our numerical computations, we also examined two auxiliary cases, when the Bragg planes are simply either contracted or expanded and when the Bragg planes are not distorted. We have also carried out many numerical simulations with different entrance-slit apertures; the above conclusion were always confirmed.

6. Conclusions

We have studied X- and γ-ray propagation in flat and cylindrically bent crystals. We have used the relevant results to describe the operation of a Laue–Laue diffractometer consisting of a flat collimating crystal and a bent analyzer crystal and we have extended the results of a previous investigation of ours (Mana *et al.*, 2004*a*). We have described the distortion characterized by a constant strain gradient in crystals having flat or cylindrical surfaces.

In both cases, in addition to numerical simulations, we have also given exact solutions of the Takagi–Taupin equations in the form of Riemann–Green integrals. We have confirmed by both analytical and numerical results that the rocking-curve shift does not depend on the shape of the analyzer surface, but only on the lattice strain on the entrance surface.

Since the validity of these solutions, *via* convolution integrals, is not limited to flat and cylindrical surfaces, we can extend such solutions either to the case when the collimating crystal is also cylindrically bent, or to the case when the effect

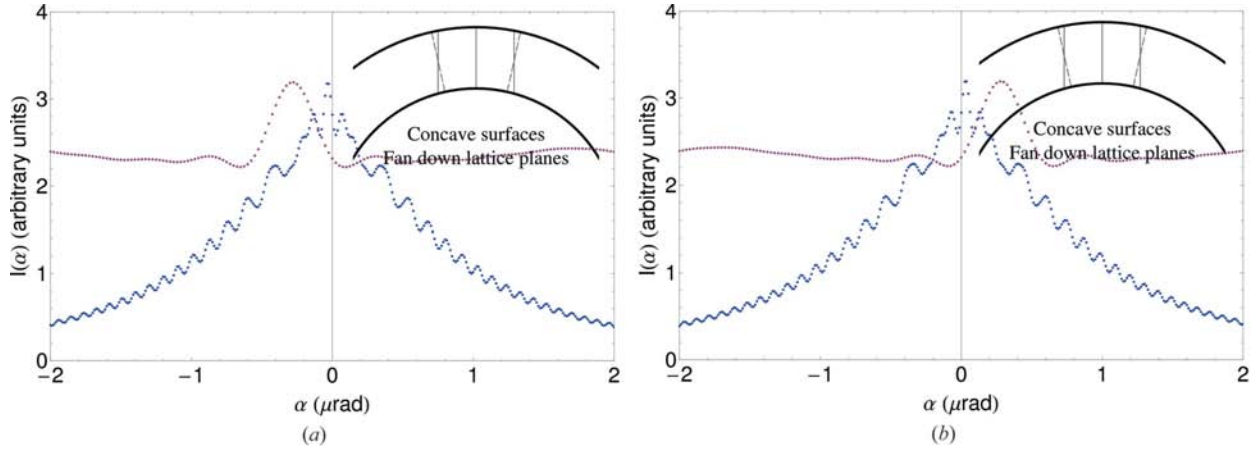

Figure 9
Non-dispersive (left) and dispersive (right) rocking curves for a concave Si analyzer with a fan-down distortion. Upper and lower curves refer to the energies of 17 keV and 184 keV, respectively. Bragg planes are (220) and the relevant parameter values are given in Table 1.

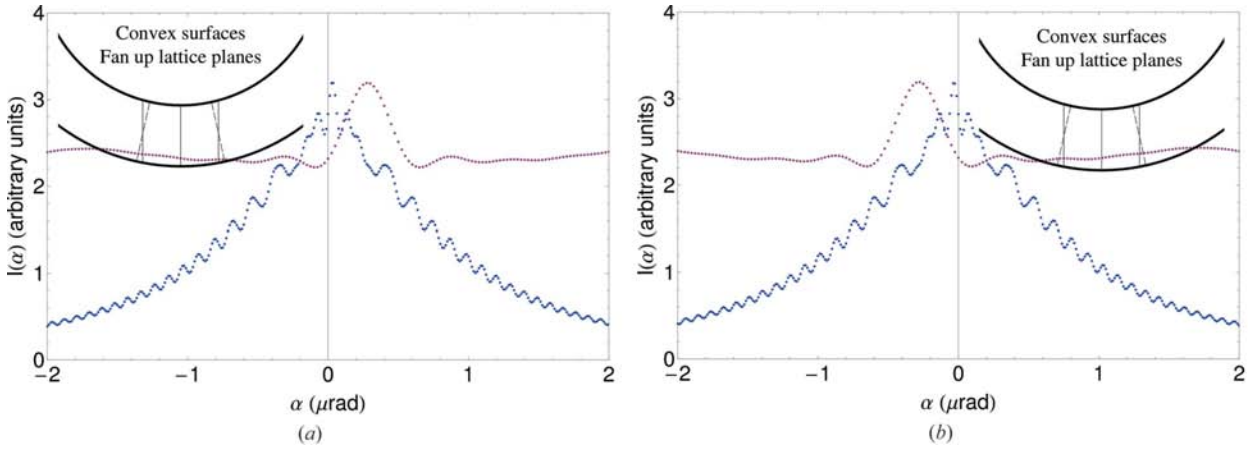

Figure 10
Non-dispersive (left) and dispersive (right) rocking curves for a convex Si analyzer with a fan-down distortion. Upper and lower curves refer to the energies of 17 keV and 184 keV, respectively. Bragg planes are (220) and the relevant parameter values are given in Table 1.

of the surface roughness in X- and γ-ray diffractometry and interferometry is not negligible. Additionally, numerical simulations open the way to a better understanding of the operation of bent-crystal diffractometers, in particular when finite-element solutions of the elasticity equations are integrated into the Takagi–Taupin equations thus allowing us to characterize the relevant lattice strains of the diffractometer crystals.

This work was supported by the Museo Storico della Fisica e Centro Studi e Ricerche 'Enrico Fermi', Rome, the Regione Piemonte and the Compagnia San Paolo, Turin. The Institut Laue-Langevin is gratefully acknowledged for beam-time allocation and support (M. Jentschel) in preliminary tests of our results.

References

Authier, A. (2001). *Dynamical Theory of X-ray Diffraction*, 2nd ed. Oxford University Press.
Authier, A. & Simon, D. (1968). *Acta Cryst.* A**24**, 517–526.
Kessler, E. (2007). Personal communication.
Mana, G. & Montanari, F. (2004). *Acta Cryst.* A**60**, 40–50.
Mana, G. & Palmisano, C. (2004). *Acta Cryst.* A**60**, 283–293.
Mana, G., Palmisano, C. & Zosi, G. (2004*a*). *Metrologia*, **41**, 238–245.
Mana, G., Palmisano, C. & Zosi, G. (2004*b*). *J. Appl. Cryst.* **37**, 773–777.
Massa, E., Mana, G. & Jentschel, M. (2005). Experiment Report 3-03-673. Institut Laue-Langevin, Grenoble, France.
Materna, T., Bruyneel, B., Jolie, J., Linnemann, A., Warr, N., Börner, H. G., Jentschel, M., Mutti, P. & Simpson, G. (2006). *Nucl. Instrum. Methods Phys. Res. A*, **569**, 890–893.
Olekhnovich, N. M. & Olekhnovich, A. I. (1980). *Acta Cryst.* A**36**, 22–27.
Palmisano, C. & Zosi, G. (2005). *Am. J. Phys.* **73**, 860–870.
Podorov, S. G. & Förster, E. (2000). *Phys. Status Solidi B*, **220**, 829–836.
Sommerfeld, A. (1964). *Partial Differential Equations in Physics*. New York: Academic Press.
Takagi, S. (1962). *Acta Cryst.* **15**, 1311–1312.
Takagi, S. (1969). *J. Phys. Soc. Jpn*, **26**, 1239–1253.
Taupin, D. (1964). *Bull. Soc. Fr. Minér. Crist.* **60**, 469–511.
Thorkildsen, G. & Larsen, H. B. (1998). *Acta Cryst.* A**54**, 172–185.
Wolfram Research (2007). *Mathematica*. Version 6.0. Wolfram Research, Inc., 100 Trade Center Drive, Champaign, IL 61820-7237, USA.